Available online at www.sciencedirect.com
SCIENCE DIRECT®
Bioorganic & Medicinal Chemistry 12 (2004) 6415–6425
Bioorganic & Medicinal Chemistry

3D-QSAR CoMFA, CoMSIA studies on substituted ureas as Raf-1 kinase inhibitors and its confirmation with structure-based studies☆

Ram Thaimattam,[a,*] Pankaj Daga,[a] Shaikh Abdul Rajjak,[a] Rahul Banerjee[a] and Javed Iqbal[b,*]

[a]*Department of Molecular Modeling and Drug Design, Dr. Reddy's Laboratories Ltd, Discovery Research, Bollaram Road, Miyapur, Hyderabad 500 049, India*
[b]*Discovery Chemistry, Dr. Reddy's Laboratories Ltd, Discovery Research, Bollaram Road, Miyapur, Hyderabad 500 049, India*

Received 23 August 2004; accepted 16 September 2004
Available online 7 October 2004

Abstract—Three-dimensional quantitative structure activity relationship (3D-QSAR) analyses were carried out on 91 substituted ureas in order to understand their Raf-1 kinase inhibitory activities. The studies include Comparative Molecular Field Analysis (CoMFA) and Comparative Molecular Similarity Indices Analysis (CoMSIA). Models with good predictive abilities were generated with the cross validated r^2 (r^2_{cv}) values for CoMFA and CoMSIA being 0.53 and 0.44, respectively. The conventional r^2 values are 0.93 and 0.87 for CoMFA and CoMSIA, respectively. In addition, a homology model of Raf-1 was also constructed using the crystal structure of the kinase domain of B-Raf isoform with one of the most active Raf-1 inhibitors (**48**) inside the active site. The ATP binding pocket of Raf-1 is virtually similar to that of B-Raf. Selected ligands were docked in the active site of Raf-1. Molecule **48** adopts an orientation similar to that inside the B-Raf active site. The 4-pyridyl group bearing amide substituent is located in the adenosine binding pocket, and anchored to the protein through a pair of hydrogen bonds with Cys424 involving ring N-atom and amide NH group. The results of best 3D-QSAR model were compared with structure-based studies using the Raf-1 homology model. The results of 3D-QSAR and docking studies validate each other and provided insight into the structural requirements for activity of this class of molecules as Raf-1 inhibitors. Based on these results, novel molecules with improved activity can be designed.
© 2004 Elsevier Ltd. All rights reserved.

1. Introduction

Cancer is considered to be one of the major killer diseases worldwide. It is caused by mutations in critical genes that alter normal cell functioning. Kinases are involved in many critical biological signaling pathways essential for the cell cycle regulation. Raf kinases, possessing serine/threonine kinase activity, are entry point to one such extracellular signal-regulated kinase/mitogen activated protein (ERK/MAP) kinase cascade. Activation of RAS–RAF–MEK–ERK signal transduction pathway initiates a cascade of events that regulates cell growth, proliferation, and differentiation in response to growth factors, cytokines, and hormones.[1] If this pathway is constantly switched on, the cell proliferation can have damaging effects, resulting in cancer.

In mammalian cells there are three members of the RAF family, A-Raf, B-Raf, and C-Raf (also termed as Raf-1). Raf-1 is a validated target for the treatment of cancer.[2] Its activation is initiated by binding to activated Ras. Activated Raf-1 in turn activates MAP kinase/ERK kinase (MEK) or MAP kinase by direct phosphorylation. MEK phosphorylates ERK or MAP kinase resulting in its activation. Ras is mutated to an oncogenic form in about 15% of human cancers.[3] More than 30 B-Raf mutations are associated with tumors.[4] Wan et al. have found that many of these mutations occurring in the kinase domain of B-Raf increase its catalytic activity either by destabilizing inactive conformation or mimicking the effect of phosphorylating the activation segment.[5] However, few mutants with impaired B-Raf

Keywords: 3D-QSAR; Homology modeling; Docking; Raf-1 kinase inhibitors.
☆ DRL Publication No. 446.
* Corresponding authors. Tel.: +91 40 2304 5439; fax: +91 40 2304 5438; e-mail: ramthaimattam@drreddys.com

0968-0896/$ - see front matter © 2004 Elsevier Ltd. All rights reserved.
doi:10.1016/j.bmc.2004.09.029

catalytic activity still stimulate ERK; they adopt a conformation that activates Raf-1, which then activates ERK. Both B-Raf and Raf-1 share highly conserved catalytic domains and downstream substrates. Therefore, inhibitors that effectively block the activity of both proteins could be useful in the treatment of broad-spectrum cancers.[6]

Benzylidine indolinones,[7] amides,[8] and triaryl imidazoles[9] have been demonstrated to inhibit Raf-1 kinase activity. Structure–activity relationship (SAR) studies of a series of potent, orally active substituted ureas led to the identification of a potent Raf-1 inhibitor, BAY 43-9006, **48** (Scheme 1), which is in the advanced stages of clinical trials.[10] Recently, Wan et al. have reported

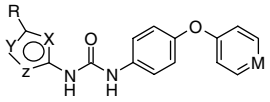

1. X = CH, Y = O , Z = N, R = t-butyl , M = CH **(5.96)**
2. X = CH, Y = O , Z = N, R = t-butyl , M = N **(6.64)**
3. X = CH, Y = N , Z = O, R = t-butyl , M = CH **(6.24)**
4. X = O, Y = N , Z = N, R = t-butyl , M = N **(5.20)**
5. X = CH, Y = N , Z = NH, R = t-butyl , M = N **(6.70)**
6. X = CH, Y = N , Z = NMe, R = t-butyl , M = N **(6.10)**
7. X = CH, Y = CH=CH , Z = CH, R = t-butyl , M = N **(6.06)**
8. X = S, Y = N , Z = N, R = t-butyl , M = N **(5.07)**
9. X = CH, Y = N , Z = O, R = t-butyl , M = N **(6.92)**
10. X = CH, Y = N , Z = O, R = isopropyl , M = CH **(5.11)**
11. X = CH, Y = N , Z = O, R = 1,1-dimethyl-propyl , M = CH **(6.15)**
12. X = CH, Y = N , Z = O, R = 1,1-dimethyl-propyl , M = N **(6.80)**
13. X = CH, Y = N , Z = O, R = Cyclobutyl , M = N **(6.06)**
14. X = CH, Y = N , Z = O, R = 1- Methyl-1-ethyl-propyl , M = CH **(5.79)**
15. X = CH, Y = N , Z = O, R = 1- Methyl-1-ethyl-propyl , M = N **(6.55)**

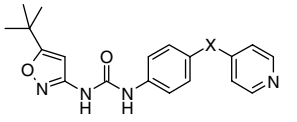

16. X = CH_2 **(6.23)**
17. X = S **(6.66)**
18. X = NMe **(5.46)**

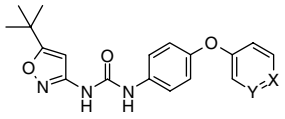

19. X = CCl, Y = CH **(5.89)**
20. X = C(Me), Y = CH **(6.00)**
21. X = C(OH), Y = CH **(6.68)**
22. X = C(NO_2), Y = CH **(5.44)**
23. X = C(OMe), Y = CH **(6.30)**
24. X = CH, Y = C(OH) **(6.57)**
25. X = C(COMe), Y = CH **(6.09)**
26. X = CH, Y = N**(6.55)**
27. X = C(CO_2H), Y = CH **(5.20)**
28. X = C(NH_2), Y = CH **(5.64)**
29. X = C(NHAc), Y = CH **(5.00)**
30. X = CH, Y = C(CO_2Et) **(5.48)**
31. X = CH, Y = C(CONHMe) **(6.92)**
32. X = CH, Y = C(OMe) **(6.15)**
33. X = CH, Y = C(CF_3) **(5.42)**
34. X = N, Y = C(Me) **(6.72)**
35. X = CH, Y = C(CO_2H) **(5.36)**

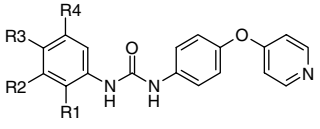

36. R_1 = H, R_2 = H, R_3 = Cl, R_4 = CF_3 **(7.34)**
37. R_1 = H, R_2 = CF_3, R_3 = H, R_4 = CF_3 **(6.22)**
38. R_1 = OMe, R_2 = Cl, R_3 = H, R_4 = H **(5.57)**
39. R_1 = Cl, R_2 = H, R_3 = H, R_4 = CF_3 **(6.35)**
40. R_1 = H, R_2 = H, R_3 = H, R_4 = CF_3 **(6.34)**
41. R_1 = OMe, R_2 = H, R_3 = NO_2, R_4 = H **(5.36)**
42. R_1 = F, R_2 = H, R_3 = H, R_4 = CF_3 **(6.14)**
43. R_1 = H, R_2 = OMe, R_3 = H, R_4 = CF_3 **(6.29)**
44. R_1 = H, R_2 = H, R_3 = H, R_4 = OCF_3 **(6.36)**
45. R_1 = H, R_2 = H, R_3 = Br, R_4 = CF_3 **(7.46)**
46. R_1 = H, R_2 = H, R_3 = F, R_4 = CF_3 **(6.28)**
47. R_1 = H, R_2 = H, R_3 = Cl, R_4 = Br **(6.35)**

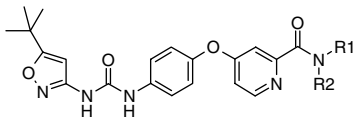

59. R_1 = H , R_2 = Me **(6.92)**
60. R_1 = H , R_2 = Et **(6.89)**
61. R_1 = H , R_2 = n-Pr **(6.85)**
62. R_1 = Me , R_2 = Me **(5.24)**
63. R_1 = H , R_2 = CH_2Ph **(6.34)**
64. R_1 = H , R_2 = Ph **(6.43)**
65. R_1 = H , R_2 = 3-Pyridyl **(7.17)**

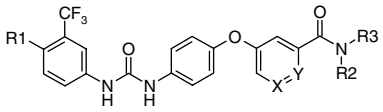

48. X = CH, Y = N, R_1 = Cl, R_2 = H, R_3 = Me **(7.92)**
49. X = CH, Y = N, R_1 = Cl, R_2 = H, R_3 = H **(7.89)**
50. X = CH, Y = N, R_1 = Cl, R_2 = H, R_3 = Et **(7.59)**
51. X = CH, Y = N, R_1 = Cl, R_2 = H, R_3 = CH_2CH_2OH **(7.55)**
52. X = CH, Y = N, R_1 = Cl, R_2 = Me, R_3 = Me **(6.52)**
53. X = CH, Y = N, R_1 = Br, R_2 = H, R_3 = Me **(8.22)**
54. X = CH, Y = N, R_1 = Br, R_2 = H, R_3 = Et **(7.57)**
55. X = CH, Y = N, R_1 = Br, R_2 = Me, R_3 = Me **(6.77)**
66. X = CH, Y = CH, R_1 = Cl, R_2 = H, R_3 = Me **(6.89)**
67. X = CH, Y = CH, R_1 = Cl, R_2 = H, R_3 = 4-Morpholinyl-$(CH_2)_2$ **(7.15)**
68. X = CH, Y = CH, R_1 = Cl, R_2 = H, R_3 = 1-Piperidinyl-$(CH_2)_2$ **(7.09)**
69. X = CH, Y = CH, R_1 = Cl, R_2 = H, R_3 = 2-Et-pyrrolidin-1-yl-(CH_2) **(6.57)**
70. X = CH, Y = CH, R_1 = Cl, R_2 = H, R_3 = 3-Pyridyl **(7.36)**
71. X = CH, Y = CH, R_1 = Cl, R_2 = H, R_3 = 4-(Me_2N)-phenyl **(6.64)**
72. X = CH, Y = CH, R_1 = Cl, R_2 = H, R_3 = PhNH-$(CH_2)_2$ **(6.80)**
73. X = CH, Y = CH, R_1 = Cl, R_2 = H, R_3 = MeO-$(CH_2)_2$ **(6.96)**
74. X = CH, Y = CH, R_1 = Cl, R_2 = H, R_3 = 4-MeO-3-pyridyl **(6.89)**
75. X = CH, Y = CH, R_1 = Cl, R_2 = H, R_3 = (4-Morpholinyl)phenyl **(6.80)**
76. X = CH, Y = N, R_1 = Cl, R_2 = H, R_3 = 4-Morpholinyl-$(CH_2)_2$ **(7.14)**
77. X = N, Y = CH, R_1 = Cl, R_2 = H, R_3 = 4-Morpholinyl-$(CH_2)_2$ **(6.85)**
78. X = N, Y = CH, R_1 = Cl, R_2 = H, R_3 = Me **(7.30)**
91. X = CH, Y = N, R_1 = Br, R_2 = H, R_3 = 4-Morpholinyl-$(CH_2)_2$ **(7.22)**

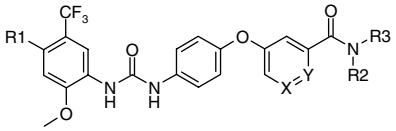

56. X = CH, Y = N , R_1 = Cl , R_2 = H , R_3 = Me **(7.39)**
57. X = CH, Y = N , R_1 = Cl , R_2 = H , R_3 = Et **(7.06)**
58. X = CH, Y = N , R_1 = Cl , R_2 = H , R_3 = i-Pr **(6.62)**
79. X = CH, Y = CH , R_1 = H , R_2 = H , R_3 = Me **(6.89)**
80. X = CH, Y = CH , R_1 = H , R_2 = H , R_3 = 3-Pyridyl **(7.00)**
81. X = CH, Y = CH , R_1 = H , R_2 = H , R_3 = 4-(Me_2N)-Phenyl **(6.39)**
82. X = CH, Y = CH , R_1 = H , R_2 = H , R_3 = 6-MeO-3-Pyridyl **(6.82)**
83. X = CH, Y = CH , R_1 = H , R_2 = H , R_3 = (4-Morpholinyl)phenyl **(6.68)**
84. X = CH, Y = N , R_1 = H , R_2 = H , R_3 = Me **(7.28)**
85. X = CH, Y = N , R_1 = H , R_2 = H , R_3 = Et **(6.34)**
86. X = CH, Y = N , R_1 = H , R_2 = Me , R_3 = Me **(6.48)**
87. X = CH, Y = N , R_1 = H , R_2 = H , R_3 = i-Bu **(6.30)**
88. X = N, Y = CH , R_1 = H , R_2 = H , R_3 = 4-Morpholinyl-$(CH_2)_2$ **(7.20)**
89. X = N, Y = CH , R_1 = H , R_2 = H , R_3 = Me **(7.21)**
90. X = N, Y = CH , R_1 = H , R_2 = H , R_3 = Me_2N-$(CH_2)_2$ **(7.00)**

Scheme 1. Molecules used for 3D-QSAR studies and their actual pIC_{50} values in parentheses.

the crystal structure of **48** bound to the kinase domain of B-Raf isoform.[5] In the present study, 3D-QSAR analyses were carried out on the series of substituted ureas as Raf-1 inhibitors in order to identify the key structural elements required to design potential drug candidates of this class.[10] The studies include Comparative Molecular Field Analysis (CoMFA)[11] and Comparative Molecular Similarity Indices Analysis (CoMSIA).[12] In addition, docking studies of selected molecules in the ATP binding pocket of a Raf-1 homology model were also carried out. The Raf-1 model was built using the crystal structure of B-raf kinase domain. Furthermore, the results of best QSAR model were compared with structure-based studies. To our knowledge, the present study—which is the first of this type—was aimed at developing 3D-QSAR models for Raf-1 inhibitors and understanding ligand–receptor interactions through structure-based studies.

2. Methods

2.1. Data set

A series of potent, orally active substituted ureas reported to have Raf-1 kinase inhibitory activities was chosen in this study (Scheme 1).[10] In vitro Raf-1 kinase activities were converted into the corresponding pIC_{50} ($-\log IC_{50}$) values. The pIC_{50} values were used as dependent variables in the CoMFA and CoMSIA analyses. The total set of Raf-1 inhibitors (91 compounds) was divided into training (71 compounds) and test (20 compounds) sets in the approximate ratio 4:1 (Tables 1 and 2). Training and test sets were selected manually such that structurally diverse molecules possessing activities of wide range were included in both sets. The pIC_{50} values of the molecules considered in this study spanned a range of 3 log units.

2.2. Molecular modeling

The X-ray coordinates of potent Raf-1 inhibitor (**48**) bound to the active site of B-Raf[5] (Protein Data Bank, PDB code: 1UWH)[13] were used as the template to construct the 3D models of all the compounds using SYBYL 6.92.[14] All structures were minimized using MMFF94[15] force fields with distance dependent dielectric constant and convergence gradient method with a convergence criterion of 0.001 kcal/mol. Atomic charges were calculated using the MMFF94 method.

2.3. Alignment

The conformation of **48** inside the active site of B-Raf was used as the template for aligning the rest of the molecules to it. Three different alignment methods, namely, atomfit, database, and multifit alignments, were carried out. The atoms selected for superimposition is shown in Scheme 2.

2.4. CoMFA and CoMSIA

The aligned training set molecules were placed in a 3D grid box such that the entire set was included in it.

Table 1. Experimental IC_{50}, pIC_{50}, predicted pIC_{50} and residual values of molecules used in the training set for CoMFA (atomfit) and CoMSIA2

Code	IC_{50} (nM)	Actual pIC_{50}	CoMFA		CoMSIA	
			Pred. pIC_{50}	Residual	Pred. pIC_{50}	Residual
1	1100	5.96	6.11	−0.15	6.05	−0.09
3	570	6.24	6.29	−0.05	6.30	−0.06
5	200	6.70	6.85	−0.15	6.73	−0.03
6	800	6.10	6.23	−0.13	6.55	−0.45
7	870	6.06	6.03	0.03	5.99	0.07
8	8600	5.07	5.44	−0.37	5.18	−0.11
9	120	6.92	6.71	0.21	6.41	0.51
10	7800	5.11	5.23	−0.12	6.02	−0.91
12	160	6.80	6.68	0.12	6.49	0.31
13	880	6.06	5.98	0.08	6.23	−0.17
15	280	6.55	6.42	0.13	6.21	0.34
16	590	6.23	6.20	0.03	6.58	−0.35
17	220	6.66	6.34	0.33	6.51	0.15
18	3500	5.46	5.31	0.15	5.57	−0.11
19	1300	5.89	6.06	−0.17	6.05	−0.16
21	210	6.68	6.48	0.21	6.60	0.08
22	3600	5.44	5.52	−0.08	5.75	−0.31
23	500	6.30	6.10	0.20	5.99	0.31
24	270	6.57	6.66	−0.09	6.75	−0.18
25	820	6.09	6.21	−0.12	5.89	0.20
26	280	6.55	6.71	−0.16	6.50	0.05
29	10,000	5.00	5.10	−0.10	5.30	−0.30
30	3300	5.48	5.37	0.11	5.37	0.11
32	700	6.15	6.53	−0.38	6.05	0.10
34	190	6.72	6.47	0.25	6.46	0.26
35	4400	5.36	5.23	0.13	5.57	−0.21
37	600	6.22	6.25	−0.03	6.32	−0.10
38	2700	5.57	5.49	0.08	5.48	0.09
39	450	6.35	6.22	0.13	6.30	0.05
41	4400	5.36	5.14	0.22	5.00	0.36
42	720	6.14	6.38	−0.23	6.31	−0.17
43	510	6.29	6.36	−0.07	6.51	−0.22
44	440	6.36	6.30	0.06	6.27	0.09
45	35	7.46	7.08	0.38	6.97	0.49
46	530	6.28	6.67	−0.39	6.65	−0.37
47	450	6.35	6.59	−0.24	6.40	−0.05
48	12	7.92	7.83	0.09	7.83	0.09
50	26	7.59	7.63	−0.04	7.30	0.29
51	28	7.55	7.50	0.05	7.58	−0.03
52	300	6.52	6.52	0.01	6.40	0.12
53	6	8.22	7.96	0.26	7.95	0.27
55	170	6.77	6.59	0.18	6.50	0.27
56	41	7.39	7.42	−0.03	7.76	−0.37
58	240	6.62	6.66	−0.04	7.00	−0.38
59	120	6.92	6.75	0.17	6.60	0.32
60	130	6.89	6.74	0.15	6.55	0.34
62	5800	5.24	5.49	−0.25	5.62	−0.38
63	460	6.34	6.10	0.24	6.23	0.11
64	370	6.43	6.85	−0.42	6.41	0.02
65	68	7.17	7.15	0.02	7.02	0.15
66	130	6.89	7.22	−0.33	7.22	−0.33
67	70	7.15	7.30	−0.15	7.15	0.00
68	82	7.09	7.28	−0.19	7.09	0.00
69	270	6.57	6.42	0.15	6.52	0.05
71	230	6.64	6.63	0.01	6.81	−0.17
73	110	6.96	7.03	−0.07	6.87	0.09
74	130	6.89	6.83	0.06	6.78	0.11
75	160	6.80	6.89	−0.09	7.04	−0.24
76	73	7.14	7.21	−0.07	7.18	−0.04
78	50	7.30	7.06	0.25	7.50	−0.20
79	130	6.89	6.90	0.00	6.78	0.11

(*continued on next page*)

Table 1 (*continued*)

Code	IC_{50} (nM)	Actual pIC_{50}	CoMFA		CoMSIA	
			Pred. pIC_{50}	Residual	Pred. pIC_{50}	Residual
80	100	7.00	6.97	0.04	6.85	0.15
81	410	6.39	6.39	0.00	6.41	−0.02
82	150	6.82	6.95	−0.13	7.10	−0.28
83	210	6.68	6.67	0.02	6.60	0.08
84	53	7.28	7.33	−0.05	7.38	−0.10
86	330	6.48	6.24	0.24	5.98	0.50
87	500	6.30	6.35	−0.05	6.29	0.01
88	63	7.20	6.97	0.23	6.91	0.29
90	100	7.00	6.92	0.08	7.02	−0.02
91	60	7.22	7.34	−0.12	7.30	−0.08

Table 2. Experimental IC_{50}, pIC_{50}, predicted pIC_{50} and residual values of molecules used in the test set for CoMFA (atomfit) and CoMSIA2

Code	IC_{50} (nM)	Actual pIC_{50}	CoMFA		CoMSIA	
			Pred. pIC_{50}	Residual	Pred. pIC_{50}	Residual
2	230	6.64	6.33	0.31	6.23	0.41
4	6300	5.20	5.64	−0.44	6.06	−0.85
11	700	6.15	6.79	−0.64	6.37	−0.22
14	1620	5.79	6.50	−0.71	6.33	−0.54
20	1000	6.00	6.27	−0.27	6.01	−0.01
27	6300	5.20	5.87	−0.67	6.18	−0.98
28	2300	5.64	6.53	−0.89	6.99	−1.35
31	120	6.92	6.21	0.71	6.14	0.78
33	3800	5.42	6.15	−0.73	5.75	−0.33
36	46	7.34	6.95	0.40	6.86	0.48
40	460	6.34	6.66	−0.32	6.46	−0.11
49	13	7.89	7.49	0.40	7.95	−0.06
54	27	7.57	7.66	−0.09	7.37	0.20
57	88	7.06	6.93	0.13	7.59	−0.53
61	140	6.85	6.92	−0.07	6.51	0.34
70	44	7.36	7.27	0.09	7.25	0.11
72	160	6.80	6.95	−0.15	7.08	−0.28
77	140	6.85	7.03	−0.18	7.29	−0.44
85	460	6.34	6.99	−0.65	6.81	−0.47
89	61	7.21	6.89	0.32	7.06	0.15

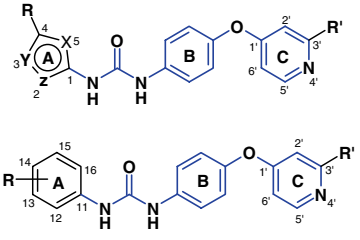

Scheme 2. Template used for molecular alignment. Highlighted atoms are used in the atomfit, multifit, and database alignments. Note that the atom numbering does not follow the IUPAC rules.

CoMFA fields were generated using sp^3 carbon probe atom carrying +1 charge to generate steric (Lennard-Jones 6–12 potential) and electrostatic (Coulomb potential) fields at each grid point. The steric and electrostatic energy values in CoMFA were truncated at 30 kcal/mol. The CoMFA fields were scaled by the CoMFA-STD method in SYBYL. The steric, electrostatic, hydrophobic, hydrogen bond donor and acceptor CoMSIA fields were derived according to Klebe et al.[12] Arbitrary definition of cutoff limits is not required in CoMSIA method, wherein a distance dependent Gaussian type functional form has been employed that takes care of abrupt changes of potential energy near the molecular surface. The default value of 0.3 was used as the attenuation factor.

The CoMFA/CoMSIA fields combined with observed biological activities (pIC_{50}) were included in a molecular spread sheet and partial least square (PLS)[16] methods were applied to generate 3D-QSAR models. The PLS algorithm with the leave-one-out[17] cross-validation method was employed to choose optimum number of components and assess the statistical significance of each model. All cross-validated PLS analyses were performed with a column filter value of 2.0. The cross-validated r^2 (r^2_{cv}) was calculated using Eq. 1.

$$r^2_{cv} = 1 - \frac{\sum(Y_{predicted} - Y_{observed})^2}{\sum(Y_{observed} - Y_{mean})^2} \quad (1)$$

where $Y_{predicted}$, $Y_{observed}$, and Y_{mean} are predicted, actual, and mean values of the target property (pIC_{50}), respectively. The optimum number of components was chosen which gave less standard error of prediction and high r^2_{cv}. To assess the predictive power of the 3D-QSAR models derived using training set, biological activities of the test set molecules were predicted. The predictive r^2 (r^2_{pred}) value was calculated using Eq. 2.

$$r^2_{pred} = (SD - PRESS)/SD \quad (2)$$

where SD is the sum of squared deviations between the biological activity of the test set and the mean activity of training set molecules, and PRESS is the sum of squared deviations between the actual and the predicted activities of the test set molecules. In addition, the r^2_{cv}, r^2_{pred} and number of components, the conventional correlation coefficient r^2 and its standard error were also computed for each model. The CoMFA/CoMSIA results were graphically interpreted by field contribution maps using the 'STDEV*COEFF' field type.

2.5. Homology modeling

The tertiary structure of Raf-1, for which a crystal structure is not available, was constructed by the method of homology modeling using the crystal structure of the kinase domain of human B-Raf isoform.[5] In homology modeling, 3D structure of homologous protein is used as a template to construct unknown structure. The amino acid sequence identity between Raf-1 and B-Raf kinase domains is about 81%. The homology model of Raf-1 peptide includes amino acid residues 343–615. The alignment of human Raf-1 (Entrez Protein: P04049)[18] and B-Raf kinase domain amino acid sequences is shown in Scheme 3.[19] The 3D structure modeling and refinements were carried out using Swiss-PdbViewer.[20] The model was finally minimized with MMFF94 force fields using SYBYL.

2.6. Docking studies

Selected molecules were docked manually in the active site of Raf-1. The crystal structure of **48** bound to B-

```
Raf-1     321  -------VSGTQEKNKIRPRGQRDSSYYWEIEASEVMLSTRIGSGSFGTVYKGKWHGDVA
B-Raf     421  PQRERKSSSSSEDRNRMKTLGRRDSSDDWEIPDGQITVGQRIGSGSFGTVYKGKWHGDVA
                      *.::::*:::. *:****  ***  .:: :. **********************

Raf-1     374  VKILKVVDPTPEQFQAFRNEVAVLRKTRHVNILLFMGYMTKDNLAIVTQWCEGSSLYKHL
B-Raf     481  VKMLNVTAPTPQQLQAFKNEVGVLRKTRHVNILLFMGYSTKPQLAIVTQWCEGSSLYHHL
               **:*:*. ***:*:***:***.**************** ** :***************:**

Raf-1     434  HVQETKFQMFQLIDIARQTAQGMDYLHAKNIIHRDMKSNNIFLHEGLTVKIGDFGLATVK
B-Raf     541  HIIETKFEMIKLIDIARQTAQGMDYLHAKSIIHRDLKSNNIFLHEDLTVKIGDFGLATVK
               *: ****:*::*****************.*****:*********.**************

Raf-1     494  SRWSGSQQVEQPTGSVLWMAPEVIRMQDNNPFSFQSDVYSYGIVLYELMTGELPYSHINN
B-Raf     601  SRWSGSHQFEQLSGSILWMAPEVIRMQDKNPYSFQSDVYAFGIVLYELMTGQLPYSNINN
               ******:*.** :**:************:**:*******::**********:****:***

Raf-1     554  RDQIIFMVGRGYASPDLSKLYKNCPKAMKRLVADCVKKVKEERPLFPQILSSIELLQHSL
B-Raf     661  RDQIIFMVGRGYLSPDLSKVRSNCPKAMKRLMAECLKKKRDERPLFPQILASIELLARSL
               ************ ******: .*********:*:*:** ::*********:***** :**

Raf-1     614  PKINRSASEPSLHRAAHTEDINACTLTTSPRLPVF----------
B-Raf     721  PKIHRSASEPSLNRAGFQTEDFSLYACASPKTPIQAGGYGAFPVH
               ***:********:**..  :  :    :**: *:
```

Scheme 3. Alignment of human C-Raf (or Raf-1) and B-Raf kinase domains. The alignment was performed using CLUSTAL.[19] Residues that are completely conserved in the two sequences are indicated by asterisk below the sequence; those that are highly conserved are indicated by colon, while similar residues are indicated by a dot.

Raf was used as the reference for docking studies.[5] Structure-based studies are reported to be useful in validating 3D-QSAR results.[21] The docked structures were then minimized using MMFF94 force fields and conjugate gradient algorithm; with a gradient convergence value of 0.05 kcal/mol, and a distance dependent dielectric constant of 4. All amino acid residues within an 8 Å radius around the ligand were minimized while treating the rest of the protein as an aggregate. Atomic charges were computed using MMFF94 method.

3. Results and discussion

CoMFA and CoMSIA 3D-QSAR models were derived using a series of potent, orally active substituted ureas possessing Raf-1 kinase inhibitory activities.[10] The chemical structures of molecules and their actual pIC_{50} values are shown in Scheme 1. Only 4-phenoxy-aryl substituted ureas were considered in this study. The data set was divided into training and test sets (Tables 1 and 2). The predictive power of the 3D-QSAR models derived using training set were assessed by predicting biological activities of the test set molecules.

The CoMFA and CoMSIA 3D-QSAR methods are based on the assumption that the changes in binding affinities of ligands are related to changes in molecular properties represented by fields. The alignment rule and the bioactive conformation are crucial variables in any 3D-QSAR analysis as both will affect outcome of statistical analysis. Three different alignments, atomfit, multifit, and database, were considered in the study. The X-ray crystal structure of **48** bound to the active site of B-Raf[5] (PDB code: 1UWH) was used as the template for the superposition of rest of the molecules; as the orientation of **48** is similar in both the Raf-1 and B-Raf active sites as will be discussed later in the docking studies. The substructure used for alignments is shown in Scheme 2.

3.1. CoMFA 3D-QSAR analysis

Steric and electrostatic CoMFA fields were generated using standard procedures.[22] Three CoMFA models using atomfit, multifit, and database alignments were considered in the final analysis. The statistical details are summarized in Table 3 (panel A). While the cross-validated r^2 for atomfit and multifit alignments are similar (0.530 and 0.508), it is lower (0.398) in case of database alignment. The conventional r^2 for multifit and database alignments are comparable (0.822 and 0.865) with five and four components, respectively, while it is higher (0.930) in case of atomfit alignment with six components. The standard error of estimation value (SEE) for atomfit alignment is better (0.186) than that of multifit and database alignments (0.293 and 0.257, respectively). The predictive r^2 value is slightly better in case of atomfit method than the other two alignment methods. The steric and electrostatic field contributions of all the three models are almost similar (~50:50) indicating equal requirement of these two fields on ligand–receptor interactions. Based on the above observations, the best CoMFA model obtained by using atomfit alignment was chosen for further analysis. The actual and predicted pIC_{50} values of the training and test sets are shown in Tables 1 and 2, respectively.

The CoMFA steric and electrostatic field contour plots obtained from atomfit alignment are shown in Figure 1. The steric interactions are represented by green- and yellow-colored contours, while electrostatic interactions are represented by red- and blue-colored contours. In the green regions of steric contour plot, bulky substituents enhance biological activity, while bulky substituents in the yellow regions are likely to decrease activity.

Table 3. Summary of various CoMFA analyses on Raf-1 selective inhibitors (Panel A), results of CoMSIA studies on Raf-1 selective inhibitors (Panel B)

Fields	Atomfit alignment	Multifit alignment	Database alignment
Panel A			
r^2_{cv} [a]	**0.530**	0.508	0.398
N[b]	**6**	4	5
r^2_{conv} [c]	**0.930**	0.822	0.865
SEE[d]	**0.186**	0.293	0.257
F-value[e]	141.937	76.091	83.44
r^2_{pred} [f]	**0.620**	0.599	0.612
Contributions[g]	0.50, 0.50	0.46, 0.54	0.48, 0.52

	S E	S E H	S E D	S E A	S E D A	S E H D	S E H D A
Panel B							
Atomfit alignment							
r^2_{cv} [a]	0.349	0.34	0.515	0.377	0.471	**0.419**	0.405
N[b]	6	1	3	6	5	**6**	3
r^2_{conv} [c]	0.799	0.415	0.718	0.779	0.806	**0.858**	0.682
SEE[d]	0.316	0.519	0.365	0.331	0.308	**0.266**	0.388
F-value[e]	42.463	48.943	56.92	37.58	54.077	64.226	48.004
r^2_{pred} [f]	0.544	0.54	0.476	0.613	0.54	**0.506**	0.546
Contributions[g]	0.23, 0.77	0.14, 0.44, 0.42	0.14, 0.56, 0.30	0.14, 0.42, 0.44	0.11, 0.33 0.19, 0.37	0.10, 0.37 0.27, 0.26	0.07, 0.25, 0.24, 0.16, 0.28
Multifit alignment							
r^2_{cv} [a]	0.338	0.349	0.505	0.322	0.441	**0.441**	0.417
N[b]	2	1	3	1	5	**6**	3
r^2_{conv} [c]	0.495	0.424	0.696	0.424	0.8	**0.866**	0.663
SEE[d]	0.486	0.515	0.38	0.515	0.313	**0.258**	0.4
F-value[e]	33.298	50.826	51.142	50.711	52.006	68.869	43.879
r^2_{pred} [f]	0.597	0.597	0.513	0.516	0.635	**0.577**	0.602
Contributions[g]	0.16, 0.84	0.14, 0.43, 0.43	0.14, 0.58, 0.29	0.13, 0.38, 0.49	0.12, 0.32, 0.20, 0.36	0.10, 0.35, 0.28, 0.26	0.07, 0.25, 0.16, 0.27
Database alignment							
r^2_{cv} [a]	0.343	0.344	0.498	0.324	**0.444**	0.409	0.405
N[b]	4	2	3	5	**5**	2	3
r^2_{conv} [c]	0.671	0.536	0.726	0.737	**0.798**	0.575	0.676
SEE[d]	0.398	0.466	0.361	0.358	**0.314**	0.446	0.392
F-value[e]	33.603	39.233	59.027	36.45	51.333	45.944	46.54
r^2_{pred} [f]	0.581	0.61	0.53	0.596	**0.557**	0.597	0.556
Contributions[g]	0.201, 0.799	0.12, 0.48, 0.40	0.13, 0.58, 0.29	0.14, 0.44, 0.42	0.11, 0.33, 0.20, 0.36	0.10, 0.38 0.35, 0.18	0.07, 0.26 0.24, 0.16, 0.27

[a] Cross-validated correlation coefficient.
[b] Optimum number of components obtained from cross-validated PLS analysis and same used in final noncross-validated analysis.
[c] Noncross-validated correlation coefficient.
[d] Standard error of estimate.
[e] F-test value.
[f] Predictive r^2.
[g] Field contributions: steric (S) and electrostatic (E) fields from CoMFA. Steric (S), electrostatic (E), hydrophobic (H), donor (D), and acceptor (A) fields from CoMSIA.

Blue-colored contours represent regions where electropositive groups increase activity, whereas red-colored regions represent areas where electronegative groups enhance activity.

The green steric contour near 14-position of ring A indicates that any bulkier substituent is preferred at this position (Fig. 1a). Thus, molecules with bulkier substituents such as Cl– and Br– (**36** and **45**) at this position are more active, while the F-atom substitution (**46**) is moderately active. The tertiary butyl group at 4-position of ring A in case of heterocyclic ureas is close to the green region. It is not clear from the yellow- and green-colored contours enclosing the amide substituent at 3′-position of ring C whether the replacement of *N*-methyl group with larger alkyl groups such as ethyl or propyl would affect activity. A similar conclusion can be drawn from their actual pIC_{50} values as well. For example, compounds, namely, **59**–**61**, possess similar Raf-1 potencies. Moderate activity of **63** is due to the fact that the *N*-benzyl group occupies one of the yellow regions.

The CoMFA electrostatic contour plot is shown in Figure 1b. The red regions near the $–CF_3$ group at 15-position of ring A indicate that any electronegative group at this position would enhance the activity. Therefore, the activity of **36** is about 10-fold higher than that of **47** wherein, $–CF_3$ group replaces Br atom. The blue region near 12-position of ring A indicates that substitution of electropositive group at this position would increase the

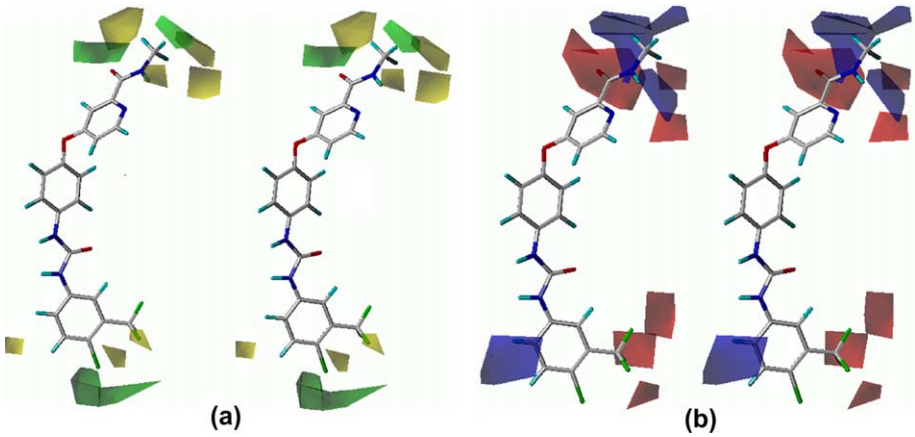

Figure 1. Stereoview of the contour plots (STDEV*COEFF) of the CoMFA (atomfit alignment) (a) steric fields; green contours indicate regions where bulky groups increase activity, whereas yellow contours indicate regions where bulky groups decrease activity and (b) electrostatic fields; blue contours indicate regions where electropositive groups increase activity, whereas red contours indicate regions where electronegative groups increase activity. Potent Raf-1 inhibitor **48** is displayed in the background for reference.

activity. Presence of red contour near 3′-position of ring C emphasizes the electronegative environment is desirable at this position. The electronegative amide group at this position is present in all potent diphenylureas. The blue region near 4′-position of ring C suggests that electropositive group substitution at this position enhances activity. The OH group at this position in **21** is near this region and hence exhibits higher activity than corresponding **1**. Molecules bearing electronegative substituents at this position are less active (**19**, **22**, and **23**).

The CoMFA steric and electrostatic contour plots and the orientation of the molecules inside the contours in case of database and multifit alignments are more or less similar to that of atomfit alignment.

3.2. CoMSIA 3D-QSAR analysis

The CoMSIA method defines explicit hydrophobic (H) and hydrogen bond donor (D) and acceptor (A) descriptors in addition to the steric (S) and electrostatic (E) fields used in CoMFA. PLS analyses of various CoMSIA models obtained using three different alignments and with different combinations of fields are shown in Table 3 (panel B). The CoMSIA model that included S, E, H, and D fields performed better than the other field combinations in case of atomfit (CoMSIA1) and multifit (CoMSIA2) alignment methods. In contrast, the model with four fields that did not include hydrophobic fields performed better in case of database alignment (CoMSIA3). The cross-validated r^2 for these three models are 0.419, 0.441, and 0.444, respectively. The conventional r^2 values for CoMSIA1 and CoMSIA2 with six components are higher (0.858 and 0.866, respectively) than that of CoMSIA3 model (0.798) with five components. While the standard error of estimation values are better in case of CoMSIA1 and CoMSIA2 (0.266 and 0.258, respectively), it is worse in case of CoMSIA3 (0.314). The predictive r^2 values of these models are 0.506, 0.577, and 0.557, respectively. The steric, electrostatic and hydrophobic field contributions for all these models are similar. There are no significant differences between CoMSIA1 and CoMSIA2 models but the PLS statistics are slightly better for CoMSIA2. Hence, CoMSIA2 was chosen for further analysis. The actual and predicted pIC_{50} values of the training and test sets for CoMSIA2 are shown in Tables 1 and 2, respectively.

In CoMSIA method, the steric fields are represented by green- and yellow-colored contours (green, bulky substitution favored; yellow, bulky substitution disfavored); the electrostatic fields are indicated by red- and blue-colored contours (blue, electropositive group favored; red, electronegative group favored); the hydrophobic fields represented by yellow- and white-colored contours (yellow, favored; white, disfavored); the hydrogen bond donor fields are indicated by cyan- and purple-colored contours (cyan, favored; purple, disfavored); while the hydrogen bond acceptor fields are denoted by magenta and red contours (magenta, favored; red, disfavored).

The CoMSIA steric and electrostatic field contour plots obtained from mutifit alignment employing S, E, H, and D fields are shown in Figure 2. These plots (Fig. 2a and b) are more or less similar to the corresponding CoMFA plots (Fig. 1a and b, respectively), except that there is an unexplained blue contour near $-CF_3$ group on ring A (Fig. 2b). Interestingly, the red CoMSIA electrostatic contour near *N*-methyl group of the amide substituent which is not present in the corresponding CoMFA plot is located on the 3-pyridyl *N*-atom of **65**. Therefore, compound **65** exhibits higher activity than corresponding phenyl analog (**64**). The hydrophobic and hydrogen bond donor contours are shown in Figure 2c and d, respectively. The yellow hydrophobic contour near 14- and 15-position of ring A (Fig. 2c) matches with the green steric contour (Fig. 2a). This indicates that any bulky group with lipophilic character is preferred at this position. The presence of cyan-colored contour near the amide NH of ring C indicates that hydrogen bond donor substituent at this position enhances the Raf-1 kinase inhibitory activity (Fig. 2d). Therefore, molecules,

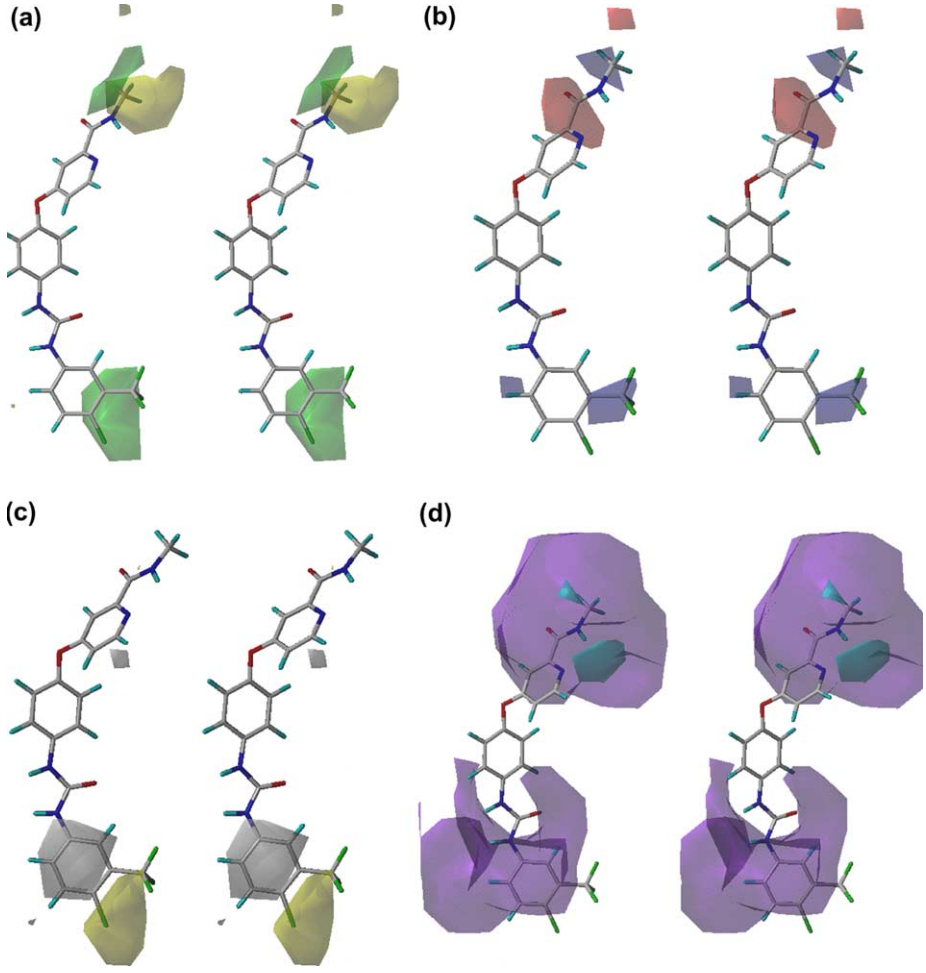

Figure 2. Stereoview of the contour plots of the CoMSIA2 (a) steric fields (green, bulky substitution favored; yellow, bulky substitution disfavored), (b) electrostatic fields (blue, electropositive group favored; red, electronegative group favored), (c) hydrophobic fields (yellow, favored; white, disfavored), and (d) donor fields (cyan, favored; purple, disfavored). Potent Raf-1 inhibitor **48** is displayed in the background for reference.

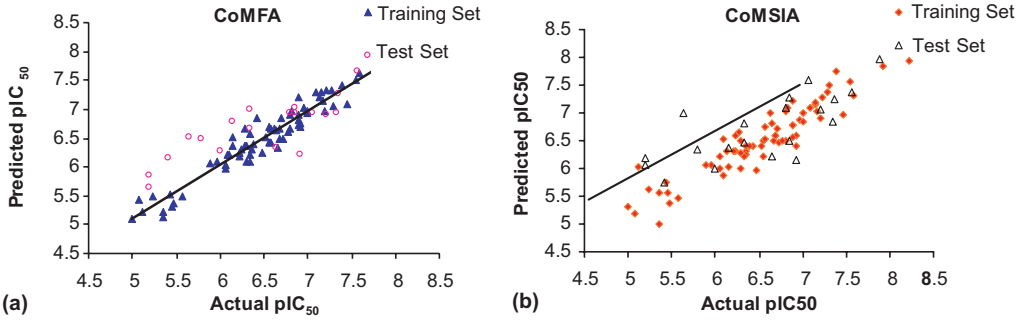

Figure 3. Actual versus predicted pIC_{50} of training and test set molecules for (a) CoMFA (atomfit alignment) and (b) CoMSIA (multifit alignment using steric, electrostatic, hydrophobic and donor fields) 3D-QSAR models.

namely, **52**, **55**, **62**, and **86** with $-N(CH_3)_2$ substitution rather than $-NHCH_3$ at this position are moderate to less active.

The steric, electrostatic, hydrophobic, and donor contour plots and the orientation of the molecules inside the contours are similar for CoMSIA1 and CoMSIA2 models. The situation is similar in case of steric, electrostatic, and donor contour plots of CoMSIA3 except that 3′-5′ positions of ring C is surrounded by a large patch of violet contour in case of acceptor fields (figure not shown).

3.3. CoMFA versus CoMSIA

The predictive power of CoMFA and CoMSIA2 3D-QSAR models were evaluated by using the test set of 20 molecules. The PLS statistics of both CoMFA and CoMSIA 3D-QSAR models indicate that CoMFA is somewhat better than CoMSIA. In both models, the

predictive values fall close to the actual pIC_{50} values, not deviating by more than 1 logarithmic unit (Fig. 3, Tables 1 and 2) except for one of the less active test set molecules (**28**) in case of CoMSIA. Molecule **28** is an outlier (residual more than 1.0) for CoMSIA, whereas in CoMFA, the residual value is quite high (0.89). Both models predicted higher activity for **28**. These values (pIC_{50}) are close to the actual pIC_{50} value of **21** but the actual activity (IC_{50}) of molecule **28** is 10-fold lower than corresponding **21**, wherein $–NH_2$ replaces –OH group. These observations indicate that a remeasurement of the activity of **28** may be useful. In summary, the differences between CoMFA and CoMSIA are not striking and both models demonstrated good predictive ability.

3.4. Docking analysis

An accurate 3D structure of target receptor is required for docking studies. Crystal structure of human Raf-1 kinase domain has not been determined. Hindley et al.[23] have constructed a homology model of Raf-1 kinase domain using the crystal structure of c-Src kinase domain in order to identify Raf-1 mutants that accept orthogonal (unable to fit into the binding site) ATP analogs. The two proteins share only 33% sequence identity in their kinase domains. Recently, the crystal structure of the kinase domain of human B-Raf isoform with potent Raf-1 inhibitor **48** inside the active site was published.[5] The sequence identity between Raf-1 and B-Raf kinase domains is about 81%. The alignment of these sequences is shown in Scheme 3. It was possible to construct a reasonably accurate homology model of Raf-1 using the crystal structure of B-raf kinase domain owing to high sequence similarity between Raf-1 and B-Raf kinase domains. The ATP binding pocket of Raf-1 homology model is virtually similar to that of B-Raf. Therefore, selected molecules were positioned in an orientation similar to that of **48** found in the active site of B-Raf prior to minimization of inhibitor–Raf-1 complexes. The hydrogen bonding interactions of **48** (Fig. 4a) in the active site of Raf-1 are similar to those present in the B-Raf active site.[5]

The 4-pyridyl ring bearing amide group (ring C) is located in the ATP adenine binding pocket by forming a pair of hydrogen bonds with Cys424 involving ring N-atom and amide NH group (ligand···receptor: N···H–N 3.66 Å; N–H···O=C 3.14 Å). The hydrogen bond between the ring N-atom and main chain NH of Cys424 is significantly long. The trifluoromethyl phenyl ring is located in the hydrophobic pocket formed between C and E helices. In addition, the urea group forms hydrogen bonds with Glu393 (N–H···Oε1 3.01 Å, N–H···Oε2 3.30 Å) and Asp486 (C=O···H–N 3.17 Å). The orientation of less active molecule, **29**, is similar to that of the highly active molecule **48** (Fig. 4b). However, molecule **29** is weakly bound. The two hydrogen bonds, essential for anchoring ligand to the protein in the adenosine binding pocket, are missing in this case as the amide bond at 3′-position of ring C is reversed with respect to that in **48**. In addition, the tertiary butyl group at 4-position of ring A is slightly moved away from the hydrophobic cleft.

The activity trends of molecules wherein the aromatic N-atom of ring C is either on 4′-, 5′-position or replaced with C–H are mixed. For example, **84** and **89** show similar activity, while molecule **76** exhibits slightly higher activity than corresponding **77**. While the activity of molecule **78** is higher than that of **66**, molecule **77** shows significantly lower activity than corresponding phenyl analog (**67**). Because of this mixed activity data, the 3D-QSAR models could not explain the observed activity trends for the above mentioned subset. This could be one of the reasons why attempts to include acceptor fields in the CoMSIA models did not improve model quality. However, the docking results of molecule, **48**, have revealed that the ring nitrogen at 4′-position of ring C and amide NH are essential for forming hydrogen bonding contacts with Cys424. Interestingly, it was noticed in the docking studies of few other potent molecules, namely, **49** and **50**, **53**, **54**, and **84**, that the hydrogen bond between ring N-atom and main chain NH of Cys424 is significantly longer by about 0.6 Å as compared to other hydrogen bonds present between ligand

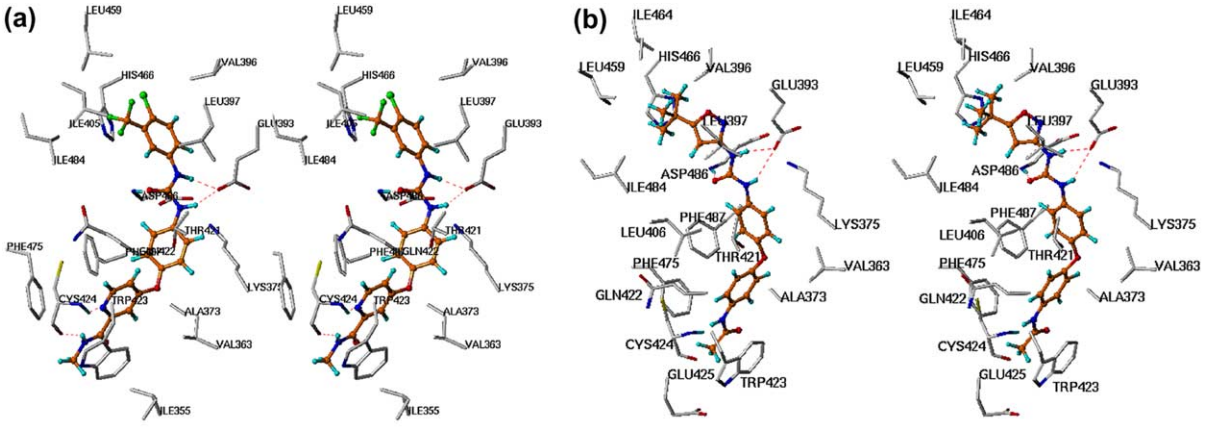

Figure 4. (a) Stereoview of the docked conformation of **48** in the active site of Raf-1. The hydrogen bonds are shown in broken lines. The ligand is shown in orange. All protein H-atoms except for the main chain NH groups of Cys424 and Asp486 are removed for clarity. (b) Stereoview of **29** Raf-1. Hydrogen bonds with Cys424 in the adenosine binding pocket are missing in the latter case. In addition, the $–CF_3$ group is embedded deeply in the hydrophobic pocket (panel a), while the tertiary butyl group is slightly moved away from the hydrophobic pocket (panel b).

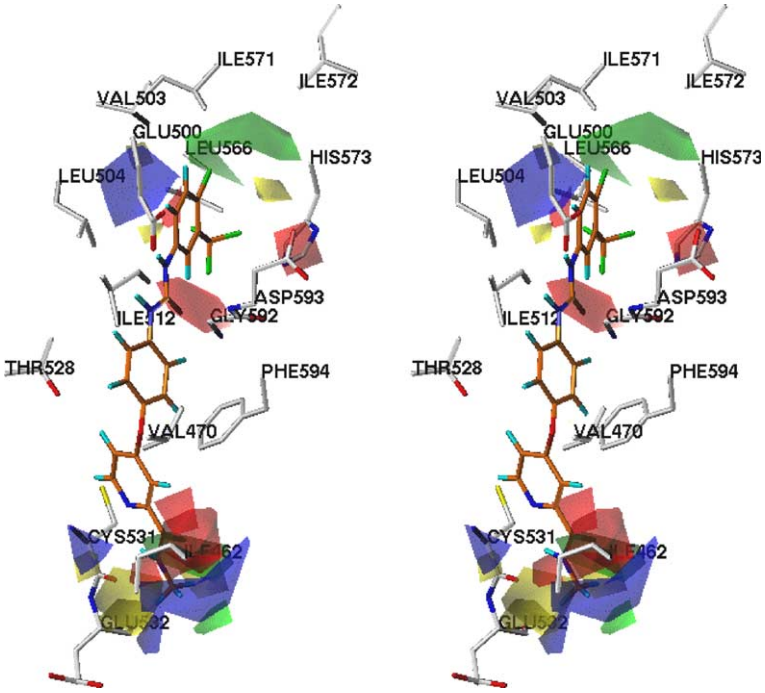

Figure 5. Stereoview of CoMFA steric and electrostatic contour plots on the ligand **48** (Fig. 1) superimposed within the active site of Raf-1.

and the protein. These observations indicate that the ring N-atom of 4-pyridyl group is involved in a relatively weak hydrogen bond with NH group of Cys424 and thus explain similar activities of 4- and 5-pyridyl analogs.

3.5. Docking versus QSAR

The overlay of CoMFA steric and electrostatic contour maps on the ligand (**48**) in the active site of Raf-1 is shown in Figure 5. The advantages of such comparisons toward a unified pharmacophore model have been reported.[21] The green contour near 14-position and red regions near $-CF_3$ group on ring A fall in the hydrophobic pocket formed between C and E helices. The aliphatic side chains of Ile405, Leu459, His466, Ile484, Val396, and Leu464 lining the hydrophobic pocket make contacts with ring A. This indicates that substituents that combine both electronegative and lipophilic properties are preferred at these positions. However, $-NO_2$ group substitution at this position may be worth exploring as it can accept C–H···O hydrogen bonds from the aliphatic side chains covering the hydrophobic pocket.[24] The large red electronegative contour near 3′-position of ring C is located in the adenosine binding pocket (Fig. 5). It is not difficult to visualize that the cyan donor contour near the amide NH also falls in this region (Fig. 2d). These observations, together with the docking results, suggest that an electronegative group bearing hydrogen bond donor at this position is required for hydrogen bonding interaction with the carbonyl O-atom of Cys424. Thus, the results of 3D-QSAR and docking studies validate each other and indicate the importance of the binding step in overall drug action. In summary, the combined analysis of CoMFA and CoMSIA 3D-QSAR and structure-based docking results was useful in explaining the SAR studies of substituted ureas which enabled us to draw meaningful conclusions.

4. Conclusions

CoMFA and CoMSIA 3D-QSAR models were developed for 91 substituted ureas as Raf-1 kinase inhibitors. Both models showed similar predictive capabilities. High degree of sequence homology between Raf-1 and B-Raf kinase domains facilitated us to construct a reasonably good homology model of Raf-1. The ATP binding pocket of Raf-1 homology model is virtually similar to that of B-Raf crystal structure. The docking studies revealed that the orientation and hydrogen bonding interactions of **48** inside the active site of Raf-1 are similar to those present in the crystal structure of **48**–B-Raf complex. The 4-pyridyl group bearing amide substituent occupies the adenosine binding pocket by forming a pair of hydrogen bonds with Cys424 involving ring N-atom and amide NH group. A comparison of the 3D-QSAR field contributions with the structural features of the binding site showed good correlation between the two analyses. To our knowledge, this is the first study aimed at deriving predictive 3D-QSAR models for Raf-1 inhibitors. In addition, the docking studies provided good insights into inhibitor–kinase interactions at molecular level. This information will be useful in the design of novel broad-spectrum anticancer drug candidates.

Acknowledgements

We acknowledge Dr. N. Selvakumar and Dr. R. Rajagopalan for their constant support and encouragement. We also thank Dr. B. Gopalakrishnan for informative discussions.

References and notes

1. Robinson, M. J.; Cobb, M. H. *Curr. Opin. Cell Biol.* **1997**, *9*, 180–186.
2. Lyons, J. F.; Wilhelm, S. M.; Hibner, B.; Bollag, G. *Endocr.-Relat. Cancer* **2001**, *8*, 219–225.
3. Malumbres, M.; Barbacid, M. *Nat. Rev. Cancer* **2003**, *3*, 459–465.
4. Davies, H.; Bignell, G. R.; Cix, C.; Stephens, P.; Edkins, S.; Clegg, S.; Teague, J.; Woffendin, H.; Garnett, M. J.; Bottomley, W., et al. *Nature* **2002**, *417*, 949–954.
5. Wan, P. T. C.; Garnett, M. J.; Roe, S. M.; Lee, S.; Niculescu-Duvaz, D.; Good, V. M.; Cancer Genome Project, Jones, C. M.; Marshall, C. J.; Springer, C. J.; Barford, D.; Marais, R. *Cell* **2004**, *116*, 855–867.
6. Morrison, D. K. *Nature* **2004**, *428*, 813–815.
7. Lackey, K.; Cory, M.; Davis, R.; Frye, S.; Harris, P.; Hunter, R.; Jung, D.; McDonald, B.; McNutt, R.; Pell, M.; Rutkowske, R.; Veal, J.; Wood, E. *Bioorg. Med. Chem. Lett.* **2000**, *10*, 223–226.
8. Hall-Jackson, C. A.; Eyers, P. A.; Cohen, P.; Goedert, M.; Boyle, F. T.; Hewitt, N.; Plant, H.; Hedge, P. *Chem. Biol.* **1999**, *6*, 559–568.
9. Heimbrook, D. C.; Huber, H. E.; Stirdivant, S. M.; Patrick, D. R.; Claremon, D.; Liverton, N.; Selnick, H.; Ahern, J.; Conroy, R.; Drakas, R.; Falconi, N.; Hancock, P.; Robinson, R.; Smith, G.; Oliff, A. 89th Meeting of the American Association for Cancer Research, New Orleans, Mar 28–Apr 1, 1998; Abstract, 3793.
10. (a) Lowinger, T. B.; Riedl, B.; Dumas, J.; Smith, R. A. *Curr. Pharm. Des.* **2002**, *8*, 2269–2278; (b) Khire, U. R.; Bankston, D.; Barbosa, J.; Brittelli, D. R.; Caringal, Y.; Carlson, R.; Dumas, J.; Gane, T.; Heald, S. L.; Hibner, B.; Johnson, J. S.; Katz, M. E.; Kennure, N.; Kingerly-Wood, J.; Lee, W.; Liu, X.-G.; Lowinger, T. B.; McAlexander, I.; Monahan, M.-K.; Natero, R.; Renick, J.; Riedl, B.; Rong, H.; Sibley, R. N.; Smith, R. A.; Wolanin, D. *Bioorg. Med. Chem. Lett.* **2004**, *14*, 783–786.
11. Cramer, R. D., III; Patterson, D. E.; Bunce, J. D. *J. Am. Chem. Soc.* **1988**, *110*, 5959–5967.
12. Klebe, G.; Abraham, U.; Mietzner, T. *J. Med. Chem.* **1994**, *37*, 4130–4146.
13. Berman, H. M.; Westbrook, J.; Feng, Z.; Gilliland, G.; Bhat, T. N.; Weissig, H.; Shindyalov, I. N.; Bourne, P. E. *Nucleic Acids Res.* **2000**, *28*, 235–242.
14. SYBYL6.92 Molecular Modeling Software, Tripos Associates, Inc.: 1669, South Hanley Road, Suite 303, St. Louis, Missouri, MO 63144-2913, USA.
15. Halgren, T. A. *J. Comput. Chem.* **1996**, *17*, 490–519.
16. (a) Dunn, W. J.; Wold, S.; Edlund, U.; Hellberg, S.; Gasteiger, J. *Quant. Struct. Act. Relat. Chem. Biol.* **1984**, *3*, 31; (b) Geladi, P. *J. Chemom.* **1988**, *2*, 231–246; (c) Wold, S. *Technometrics* **1978**, *4*, 397.
17. Cramer, R. D., III; Bunce, J. D.; Patterson, D. E. *Quant. Struct.-Act. Relat.* **1988**, *7*, 18–25.
18. Bonner, T. I.; Oppermann, H.; Seeburg, P.; Kerby, S. B.; Gunnell, M. A.; Young, A. C.; Rapp, U. R. *Nucleic Acids Res.* **1986**, *14*, 1009–1015.
19. Higgins, D. G.; Sharpe, P. M. *Gene* **1988**, *73*, 237–244.
20. Guex, N.; Peitsch, M. C. *Electrophoresis* **1997**, *18*, 2714–2723.
21. (a) Sippl, W.; Höltje, H. D. *J. Mol. Struct. (Theochem)* **2000**, *503*, 31; (b) Buolamwini, J. K.; Assefa, H. *J. Med. Chem.* **2002**, *45*, 841–852; (c) Desiraju, G. R.; Gopalakrishnan, B.; Jetti, R. K. R.; Nagaraju, A.; Raveendra, D.; Sarma, J. A. R. P.; Thilagavathi, R.; Sobhia, M. E. *J. Med. Chem.* **2002**, *45*, 4847–4857.
22. Clark, M.; Cramer, R. D., III; Jones, D. M.; Patterson, D. E.; Simeroth, P. E. *Tetrahedron Comput. Methodol.* **1990**, *3*, 47–59.
23. Hindley, A. D.; Park, S.; Wang, L.; Shah, K.; Wang, Y.; Hu, X.; Shokat, K. M.; Kolch, W.; Sedivy, J. M.; Yeung, K. C. *FEBS Lett.* **2004**, *556*, 26–34.
24. Desiraju, G. R.; Steiner, T. *The Weak Hydrogen Bond*; Oxford University Press: Oxford, 1997.